# Boundary Layer Development Downstream a Normal Shock in Transonic Intakes at Incidence

A. Coschignano* and H. Babinsky†
*Department of Engineering, University of Cambridge, Cambridge, CB2 1PZ, UK*

**The flow field around five transonic inlet lips at high incidence is investigated for a variety of flow conditions around a design point representative of high incidence manoeuvring. Changes to the operating point are simulated by varying the angle of incidence and the mass flow rate over the lip, intended to mimic the effect of an increase in engine flow. For these inflow conditions, the flow on the lip is characterised by a supersonic region, terminated by a near-normal shock wave. Of particular interest is the effect of lip geometry and operating point on the boundary layer at the equivalent fan location.**

**The parametric investigation revealed a significant effect of lip shape on the position and severity of the shock wave-boundary layer interaction. From correlation studies, it appears that the extent of shock-induced separation is the main factor affecting the boundary layer state downstream of the normal shock wave-boundary layer interaction. Somewhat surprisingly, this was found to be independent of shock strength.**

## Nomenclature

| | |
|---|---|
| $\alpha$ | Angle of incidence |
| $\delta$ | Boundary layer thickness |
| $\delta^*$ | Boundary layer displacement thickness |
| $\theta$ | Boundary layer momentum thickness |
| $c$ | Intake chord length |
| H | Shape factor |
| $L^*$ | Interaction length |
| $\dot{m}$ | Mass flow |
| $m(x)$ | Super ellipse $x$ exponent |
| M | Mach number |
| $n$ | Super ellipse $y$ exponent |
| P | Pressure |

*Research Associate, Department of Engineering, University of Cambridge.
†Professor of Aerodynamics, Department of Engineering, University of Cambridge, AIAA Associate Fellow.

$Re$ Reynolds number (based on lip thickness)

$R_c$ Inlet highlight radius of curvature

$s$ Stream-wise distance along surface; origin at the lip highlight

$t_m$ Intake thickness at the throat

$U$ Flow velocity

$x$ Stream-wise direction, parallel to lab floor

$y$ Vertical direction, normal to surface model, unless otherwise stated

$z$ Span-wise direction.

AR Intake aspect ratio

LDV Laser Doppler velocimetry

PSP Pressure sensitive paint

SBLI Shock-wave boundary layer interaction

$VEP$ Virtual Engine Plane at x=2.4$t_m, baseline$

*Subscript*

0 Stagnation value

1 Property upstream of the shock

$e$ Free-stream property

$l$ Lower channel, usually referred to mass flows

$i$ Incompressible property

$u$ Upper channel, usually referred to mass flows

## I. Flow distortion in inlets at incidence

During off-design aircraft manoeuvring at high angle of incidence the flow field over the inlet lower lip may undergo severe distortion. The flow stagnates on the outer surface of the nacelle and, as incidence or mass flow rate increase, separation may occur in the diffuser or at the highlight (inlet leading edge)[1]. Furthermore, for high mass flow rates, the formation of normal shock waves near the throat can lead to boundary layer separation and consequent total pressure losses, as schematically depicted in Figure 1[1, 2].

In recent years, in order to increase aerodynamic efficiency, manufactures are pursuing slimmer nacelles to reduce form drag during cruise. However, earlier analytical studies [3] and experiments [1, 2, 4] showed a significant effect of lip geometry and inlet contraction on the Mach number distribution over the lower lip during high incidence conditions. Due to the inability of analytical models to account for complex phenomena such as SBLI and the poor resolution of

many experiments, the effect of the geometry on the nature of the shock wave-boundary layer iteration, and its effect on the subsequent boundary layer development downstream remains to be addressed. As this boundary layer is ingested by the turbofan, minimising momentum losses might lead to a greater overall pressure recovery at the fan face.

Historically, experimental investigations of nacelle flow have been conducted using realistic three-dimensional configurations [1, 2, 4]. This prevented the use of both qualitative and quantitative techniques that rely on optical access. To overcome this problem, the current investigation uses a simplified two-dimensional approach. This provides unprecedented optical access and allows a more economical replacement of the lip geometry, facilitating parametric surveys. A total of five inlet shapes are considered in this investigation: a representative baseline inlet shape (amply discussed in a previous paper [5]) and four lip variations. Their geometry definition is discussed in §II.E. These shapes are designed to provide five different surface pressure distributions. Furthermore, two angles of incidence and mass flow rates are explored whilst maintaining a constant free-stream Mach number. Exploring the relationship between the pressure distribution and boundary layer state, this paper does not attempt to establish an optimal inlet design but rather to identify the main drivers affecting the boundary layer recovery downstream of the normal shock wave-boundary layer interaction during high-incidence manoeuvring. Ideally, the conclusions from this investigation can provide useful design criteria to inlet designers and represent a solid validation base for design methods more suited to large parametric sweeps and geometry optimisation.

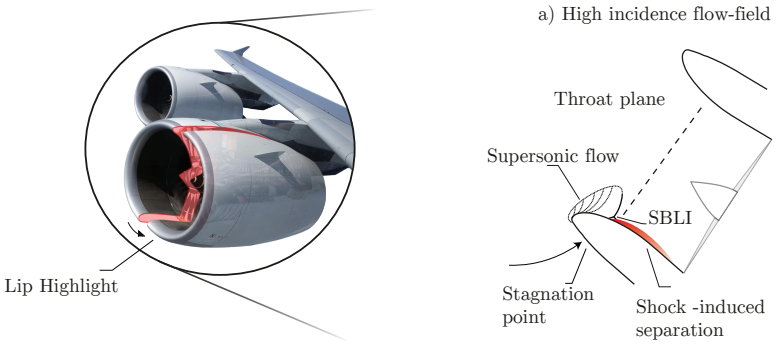


**Fig. 1 Schematics of an inlet cross section during high incidence flight: a) Separated shock wave-boundary layer interaction over the lower lip.**

## II. Methodology

### A. Target flow-field and working section design

At high incidence the main area of aerodynamic interest is around the sole lower lip. In order to simplify the problem further, the three dimensional effects along the nacelle circumference are hereby neglected. This relies on the assumption that the length-scale of tangential changes along the nacelle circumference is of the order of its curvature radius and thus noticeably larger than the lip radius and thickness, which could be considered representative length-scales

of the stream-wise and normal changes along the lip. Thus, only a cross section along the centre span of the intake is considered and the lower lip is treated like a two dimensional (2-D) aerofoil.

To delineate the experimental domain, a stream-tube was extracted in the symmetry plane from three-dimensional (3-D) *Reynolds Averaged Navier-Stokes* (RANS) computations of a typical engine flow. This defines the wind tunnel working section depicted in Figure 2. Subsequently, the set-up was fine tuned, as described in detail in §II.C, in order to obtain a pressure distribution matching experimental tests on a 3-D nacelle deemed representative of high-incidence manoeuvring and defining the current experiment baseline.

The baseline lip geometry used here is a generic lip shape (defined in §II.E) designed to generate a pressure distribution, shock strength and location comparable to the aforementioned 3-D nacelle tests. Despite the geometry simplifications the flow-field reproduced here is indicative of a cross section of the full 3-D scenario as the tangential effects are expected to have only a small impact on the supersonic region and the shock position. However, as a consequence of the absence of any pressure gradient 'relief' along the nacelle circumference, a slightly greater shock-induced separation is excepted in the 2-D case.

### B. Cambridge University Engineering Department blow down wind-tunnel

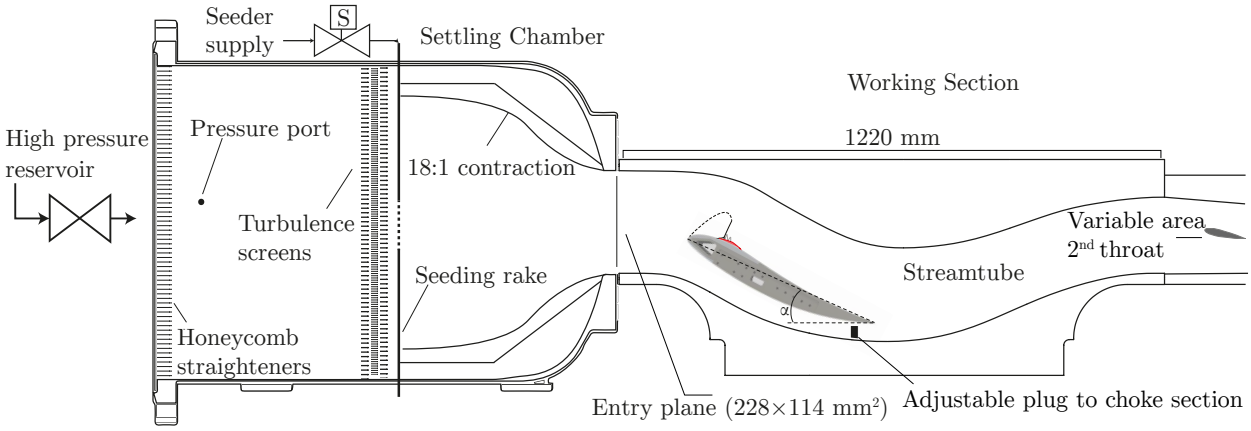


**Fig. 2 Representation of the blow-down wind tunnel facility. Flow from left to right. As seen in [5].**

The blow-down wind-tunnel assembly is schematically depicted in Figure 2. The wind-tunnel is powered by two 50 kW compressors. The flow is fed from the compressors into the settling chamber, where it is passed through a number of flow straighteners and turbulence grids before a 18:1 contraction. The working section entry area is $h \times w$ = 228×114 mm$^2$ and the entry Mach number is varied by adjusting the effective area of the second throat where the flow is choked by means of an aerofoil (see RHS of Figure 2). The working section is 1220 mm long. Changing the total pressure allows some degree of variation in Reynolds number.

The model is 444 mm long and divides the working section into two channels, bounded by the solid upper and lower walls. Altering the ratio between the mass flow rates in each channel provides an effective way to control a third variable:

the engine mass flow demand. In a real intake, when engine mass flow rate varies, so does the stagnation streamline dividing the flow entering the intake from that spilled along the outer nacelle. During high incidence operation, this streamline comes to rest on the outer surface of the lip. As the amount of air captured by the intake increases, the stagnation streamline shifts further down onto the lower surface. In the experimental facility, this is replicated by using a choking rod in the lower channel as highlighted in Figure 2. The latter allows a fine control ($\Delta\dot{m}_l < 0.1\%\dot{m}$) of the mass flow discharged via the lower passage. To investigate the response to stagnation streamline changes, the overall mass flow is kept constant at the reference value while the mass flow rate through the lower passage is progressively reduced. This forces a greater proportion of the mass flow inside the upper channel, effectively mimicking a greater demand by a turbofan engine. An increase in $\dot{m}_u$ by $15 \pm 0.3\%$ over the reference value has been considered here. The model incidence is varied between 23° and 25°.

### C. Matching the target flow-field - Reference operating conditions

This section presents the operating parameters of the current facility that result in a flow-field closely matching a typical high-incidence condition for the baseline geometry.

A Reynolds number (based on maximum thickness and inflow velocity) $Re_t \approx 1.10 \times 10^6$, representative of a full scale, small sized engine operating at sea level, is used to achieve a good compromise between dynamic similarity and run time. This value is obtained with a stagnation pressure of 211kPa. To match the 3-D test pressure distribution around the lip region, the model incidence was set at 23° and the entry Mach number to $M_\infty = 0.435 \pm 0.0005$. These are both indicative of edge of the envelope high incidence operations. The choking rod is set so that ~74% of the total mass flow is discharged via the upper channel. The operating conditions are summarised in Table 1. Reynolds number and entry Mach number are kept constant for every scenario herein investigated.

A number of off-design conditions and lip profiles are explored. However, for practical reasons the geometry of the stream-tube defining the working section, based on stream-lines of the baseline flow-field extracted from a RANS computational solution, was kept constant throughout the whole investigation. It can be argued that every operating point requires a new stream-tube geometry as the flow streamlines may change. Although an effect of the stream-tube geometry might be expected, this should not affect the main conclusions since at the design stage the upper bound of the working section was chosen to be sufficiently far from the supersonic region [6].

Furthermore, the changes in operating conditions around the design point are relatively minor: the highest increase in incidence from the baseline value is of only 2°. Moreover, the maximum increase in upper channel mass flow rate is limited to 15% of the initial value. Finally, the changes in the flow-field across the shapes tested is not so drastically different to suggest a reshaping of the wall to be necessary.

**Table 1 Inflow conditions for the reference scenario.**

| Parameter | Values |
|---|---|
| $\dot{m}$, kg/s | 8.68 |
| $M_{entry}$ | 0.435±0.005 |
| $\alpha$, deg. | 23 |
| $P_0$, kPa | 211.6 |
| $T_0$, K | 290±4 |
| $\frac{\dot{m}_u}{\dot{m}_l}$ | ~3.8 |
| $Re_t$ | $\sim 1.1 \times 10^6$ |

### D. Experimental methods and errors

A Schlieren technique is used to visualize the features typical of compressible flow-fields. A horizontal knife edge is used and the images were captured at a rate of 4000fps at a resolution of 1024×512 pixels. The Schlieren images have been averaged over 0.5 s. A longer time window does not yield noticeable differences whilst increasing the processing time.

Surface pressure measurements in the centre-span are taken using tappings connected via tubing to a differential pressure transducer. Though only 0.5 mm in diameter, the presence of a cavity can result in an over-prediction of static pressure by approximately 0.5%-1.0% according to Meier [7].

A number of these pressure readings are used to calibrate pressure sensitive paint (PSP). According to Gregory *et al.* [8], a minimum of 5 different known pressure values are usually sufficient to minimise error. In the current investigation, the mean deviation between the values extracted form the paint and that measured using the surface taps is found to range from approximately 2% to a maximum of 4%.

Flow velocities in the tunnel centre-span are measured using a two component Laser Doppler Velocimetry (LDV) system. The ellipsoidal working volume measures 130$\mu$m in diameter. Paraffin particles, with a diameter of approximately 0.5$\mu$m [9], are used to seed the flow. The laser emitting head and receiving optics are mounted on a three-axis traverse. The signal is sampled at an optimised variable rate to exploit a full signal cycle leading to a typical measurement accuracy, as stated by the manufacturer, of ±0.1% of $U_{max}$ (~580m/s) [10]. In addition the emitting head is oriented at an angle $\beta$ = 8.5° from the horizontal. A component of the span-wise velocity, $w$, therefore affects the measurement of vertical velocity component. On the symmetry plane, where measurement are taken, $w$ is expected to be one order of magnitude lower than $v$. As a consequence of this and of the small angle, the error in $v$ is expected to be just above 1%. The stream-wise velocity component $u$ is unaffected by $\beta$.

The other source of uncertainty is related to velocity bias, which According to the findings of both McLaughlin *et al.* [11] and Buchhave *et al.* [12], the error is expected to be between 5% and 10% of $U'$. In the current investigation this error is accounted for by using residence time (as recorded by the anemometer) weighted averaging as proposed by

Buchhave *et al*. [12].

Velocity measurements are used to estimate the incompressible boundary layer integral properties, which relies on integration of the velocity profile from the wall to the boundary layer edge. However, the measurement probe is of finite size and measuring any closer than 0.2mm from the wall is infeasible. Furthermore, numerically integrating over discrete data points can yield significant error. To address these shortcomings, an analytical boundary layer profile is fitted to the data points before integration.

The model by Sun & Childs [13], which builds on the classical linear combination of the law of the wall and Coles' wake function [14], has been used in the Cambridge facility for several years. Sun & Childs's model is valid down to $y^+ \approx 100$. For the buffer and viscous layers, the relationship proposed by Musker is used [15] to obtain a complete solution for $0 \leq y \leq \delta$. The incompressible integral parameters, which are preferred to their compressible counterparts as the latter are a strong function of Mach number, are then calculated by simple numerical integration. A comprehensive investigation of the validity of this method has been performed by Titchener *et al*. [16]. The main sources of errors were found to be the resolution of discrete data points and misalignment of the wall position. In particular, the number of points necessary for the error to be $\leq 5\%$ is inversely proportional to the boundary layer shape factor a minimum of 20 inside the boundary layer are sufficient to achieve an error under 5% for a range of shape factors. This condition is generally satisfied in this investigation. Overall, the error is expected to be $< 2\%$ for the largest kinematic shape factor and $< 5\%$ for the thinnest, healthiest, boundary layers.

Wall offset was found to cause a significant error in integral parameters [16]. A small misalignment of $\Delta y/\delta$ of the order of 0.01 yields an error exceeding 5%. For the thinnest boundary layer, defined by a thickness $\delta = 1.98$ mm, the wall location is accurate within $\Delta y/\delta \leq 0.005$. This places the outer error boundary to $\epsilon \leq 2\%$.

A summary of experimental error is given in Table 2.

### E. Intake Lip Design

Due to constraints on wind tunnel time, it was decided to investigate one baseline shape and four variants. These include two highlight and two aspect ratio variations over the baseline, as depicted in Figure 4. The inlet lip shapes have been designed by using a modified super ellipse profile. Mathematically, a modified super ellipse is defined as:

$$\left(\frac{x-a}{a}\right)^m + \left(\frac{y}{b}\right)^n = 1 \tag{1}$$

with

$$m_{(x)} = 2 + \left(\frac{x}{a}\right)^2 \tag{2}$$

where $a$ and $b$ are the major and minor axis of the ellipse, respectively controlling the position and the size of the

**Table 2 Summary of experimental uncertainties**

| Flow property | Source | Error |
|---|---|---|
| Stagnation pressure $P_0$ | | |
| | pressure transducer | ±0.05% |
| | settling chamber velocity (8m/s) | −0.04% |
| Static pressure $P$ | pressure transducer | ±0.05% |
| | orifice geometry - subsonic | ±0.50% |
| | orifice geometry - supersonic | ±1.00% |
| | pressure sensitive paint | ±2.00% |
| Velocity | LDV processor resolution | ±0.0015% |
| | Doppler frequency detection | ±0.10% |
| | emitter angle, $u$ | N/A |
| | emitter angle, $v$ | ±1% |
| Incompressible integral parameters $\delta_i^*$, $\theta_i$ (after [16]) | Number of discrete measurements | ±2 − 5% |
| | Wall misalignment | ±2% |

intake throat. Figure 3 depicts the coordinate system (originating at the lip highlight) and illustrates how the parameters defined in Equation 1 relate to the design of the intake lip model. The ratio $a/b$ is defined as the aspect ratio $AR$ of the ellipse. Its powers, on the other hand, set the locus of the point of maximum curvature.

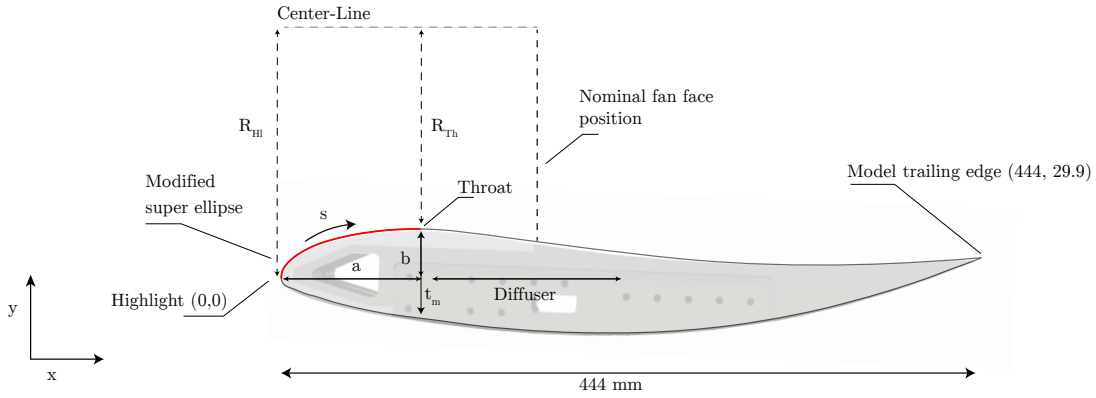


**Fig. 3 Cross section of the model depicting the intake geometry definition, modified super ellipse in red. Coordinate s is defined as arc length along the lip.**

This type of ellipse results in a continuous reduction in curvature from the highlight to the throat. Downstream of this, and up to the nominal fan location, the geometry was tailored to replicate a typical diffuser shape. This is identical for the lip profiles defined by a varying highlight sharpness but varies slightly across different aspect ratio lips to ensure a uniform curvature distribution. The mean diffuser angles, measured between the nominal fan face and the throat, range between -3.85° to -6.11° from the horizontal.

The surface contour between the nominal fan position and the trailing edge was designed using a second order polynomial and ensuring matching curvature at the nominal fan position with the rest of the intake. The trailing edge is

located at a height of 29.9 mm above the highlight, as shown in Figure 3. The external fore-body geometry is the same for every lip tested herein. The first 10% (based on chord length) of the external profile is based on a generic intake geometry; the remaining 90% is defined by a third degree polynomial up to the model trailing edge. The camber line has a minimum coordinate of -0.75 mm at a stream-wise coordinate x= 218 mm.

The baseline lip is defined by an aspect ratio $AR = 2.75$ and a value of $n = 2$. The intake thickness at the throat is $t_m = 57.8$ mm (note that this is not necessarily the maximum thickness of the assembly). The geometry definition for each shape is given in Table 3.

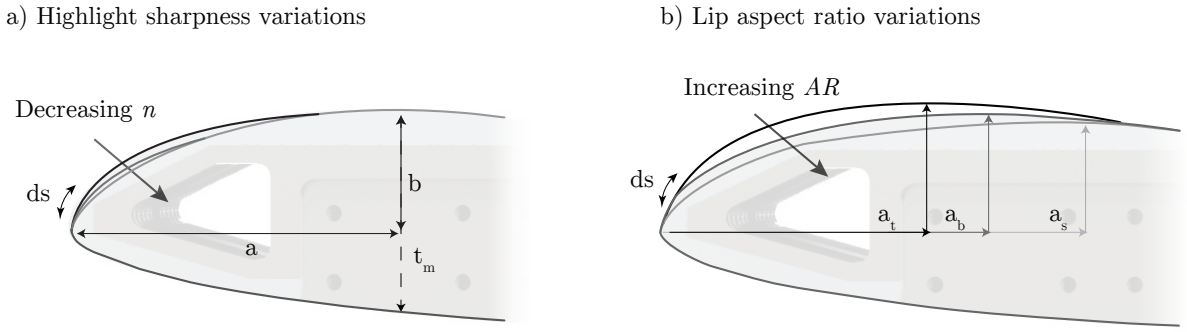


**Fig. 4 a) Lip highlight geometries obtained by changing the super ellipse exponent $n$ b) Lip geometries obtained by changing the super ellipse aspect ratio. Geometry definition provided in Table 3.**

**Table 3 Geometry definition for constant aspect ratio lips**

| Profile | $n$ | $AR$ | $R_{c\|LE}$(mm) | $t_m$ |
|---|---|---|---|---|
| Baseline | 2 | 2.75 | 5.5 | 57.8 |
| *Sharp* | 1.7 | 2.75 | 3.1 | 57.8 |
| *Blunt* | 2.2 | 2.75 | 7.0 | 57.8 |
| *Slim* | 2 | 3.63 | 4.3 | 58.6 |
| *Thick* | 2 | 2.10 | 9.3 | 59.8 |

## III. Results

### A. Flow topology response to geometry changes

Time averaged (across 0.5s) Schlieren photographs of the highlight region for the five shapes and two incidences of 23° and 25° are shown in Figure 5 and Figure 6 respectively, providing a first qualitative view of the flow field. With the exception of the *sharp* lip at the reference incidence (Fig. 5a-top), all lip flow fields are broadly defined by similar flow features. Around every lip highlight, the flow undergoes rapid acceleration and a pocket of supersonic flow is formed. This corresponds to the brighter region near the front of the lip. This supersonic region is terminated by a near-normal shock wave, visible as a dark line in the Schlieren images. At an incidence of 23°, a $\lambda$-shock structure, indicative of shock-induced separation, is not immediately obvious from the Schlieren. A smearing of the shock foot at the wall is

only observed for the high aspect ratio *slim* lip. However, in a previous investigation of the baseline lip (i.e.: Figure 5b), despite the Schlieren showed no obvious sign of shock-induced separation, a small recirculating region was observed using oil flow visualisation [5]. Thus, the inability to observe a $\lambda$-shock structure does not exclude the presence of a small separation.

Downstream of the shock, the boundary layer can be seen to grow along the surface.

From this first qualitative overview, the lip shape appears to have a noticeable influence on the position of the shock wave. Looking in detail at the peculiar sharp lip at the reference incidence, in Figure 5a-top, three shock waves are seen. The first is found in the immediate proximity of the highlight; two subsequent expansion stages follow, terminated by as many normal shock waves. The last terminal shock wave appears very weak and located further downstream compared to other inlet profiles.

Aspect ratio appears to have a strong effect on the shock position. For the highest AR *slim* lip, the shock wave is noticeably upstream, when compared to the baseline, and sits close to the highlight. On the other hand, the shock sits closer to the throat plane for the lowest aspect ratio *thick* lip. The averaged images for this shape show a modest smearing of the shock; which suggests a degree of shock unsteadiness. The standard deviation of the shock oscillation, extracted from high-speed Schlieren videos, for the *thick* lip is if $\sigma_T$ =4.48 mm, approximately 6 times the baseline value $\sigma_B$ =0.74 mm.

At the higher incidence of 25°, a flow field defined by a single shock is observed over every lip considered. However, the *slim* lip displays multiple secondary shocklets as a result of the large scale shock-induced separation. A greater smearing of the interaction is seen at 25° compared to 23° for every geometry considered, suggesting a more pronounced shock motion as incidence is increased further. Compared to the baseline, the terminal shock for the *sharp* lip is further downstream. On the other hand, the shock over the *blunt* lip profile sits upstream compared to both the baseline and same shape at lower incidence.

The flow over the *slim* lip at 25° appears to separate very close to the highlight, where a thickening of the boundary layer is observed from Schlieren. The onset of this thickening corresponds roughly with the front leg of a $\lambda$ shock, which is now large enough to be resolved by Schlieren imaging. From Figure 6c (bottom), the position of the shock over the thicker nose appears similar to the reference incidence of 23°. A more smeared shock is however seen.

Wall pressure measurements, obtained using PSP, are shown in Figures 7-8 for incidence levels of 23° (top) and 25° (bottom) respectively. The pressure along the centre-span of the model is given in Figure 9. For the *sharp* lip, the first shock very close to the highlight could not be resolved by PSP.

With the only exception of the peculiar *sharp* lip, from Figure 9 it can be seen that every flow scenario is defined by a single pressure rise across the shock. The pressure ratio (exuding the weak terminal compression over the *sharp* lip), defined as the pressure value at the sonic line (P*=0.528) over the pressure immediately upstream of the shock, ranges from $\approx$ 1.8 to $\approx$ 2.7 for the most severe cases. Oil flow visualisation for the *sharp* lip at 23° and reference mass flow

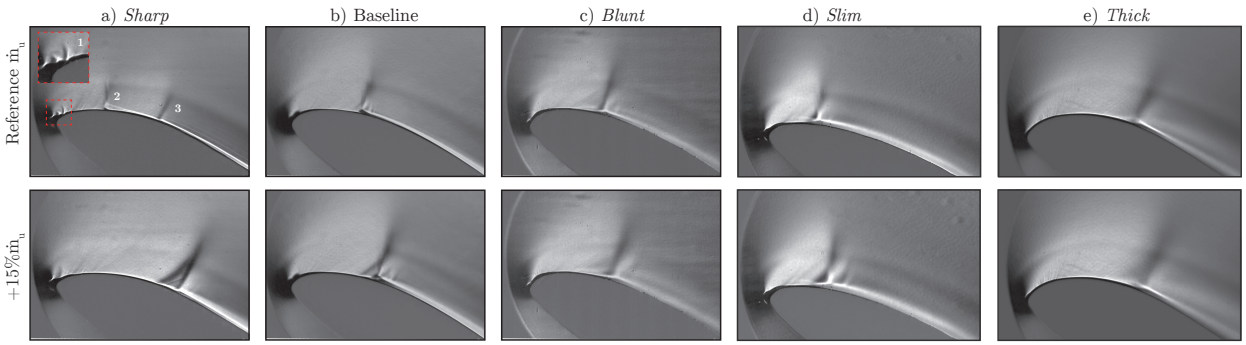


**Fig. 5 Time averaged (~0.5 s) Schlieren images for the five shapes at 23° and two mass flow rates.**

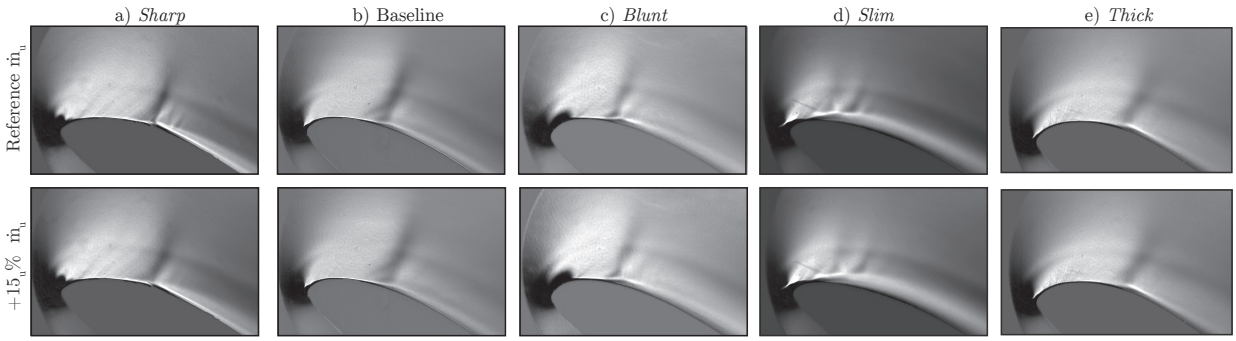


**Fig. 6 Time averaged (~0.5 s) Schlieren images for the five shapes at 25° and two mass flow rates.**

rate (see Appendix A), confirms the presence of incipient separation for the central shock-boundary layer interaction. From Figure 9, the latter has one of the weakest pressure ratios, just in excess of 1.8, and along with the *slim* lip is the weakest shock reported. Thus, based on this evidence, some degree of shock-induced separation is expected over each lip for every flow condition. Furthermore, in a previous investigation [5], it was shown how, for a number of flow conditions, the distance between the onset of pressure rise and the sonic line can provide a reasonable upper bound of the separation size (i.e.: a larger separation 'spreads' the pressure rise over a greater stream-wise distance). As an example, if this criteria were to hold here, looking at Figures 7-8, it could be concluded that the separation over the *thick* lip at 23° is seemingly larger than for the other lips.

As the incidence is increased to 25°, for the baseline case the onset of pressure rise in the centre-span is found at a stream-wise position along the surface $s_s \approx 0.9t_m$. This is similar to the baseline incidence. However, comparing Figure 7 and Figure 8, the estimated mean separation size is expected to have grown in size as there is an increasingly greater smearing of the pressure rise. Furthermore, a more extensive region of smeared pressure near the corners is observed at higher incidence.

At 25° the SBLI over the *blunt* lip exhibits an upstream shift of the shock compared to the reference incidence, as previously observed in the Schlieren images in Figure 6. The distance between the sonic line and the *blunt* lip centre-line pressure rise onset is greater than the reference incidence, implying extensive separation. Wall pressure measurements

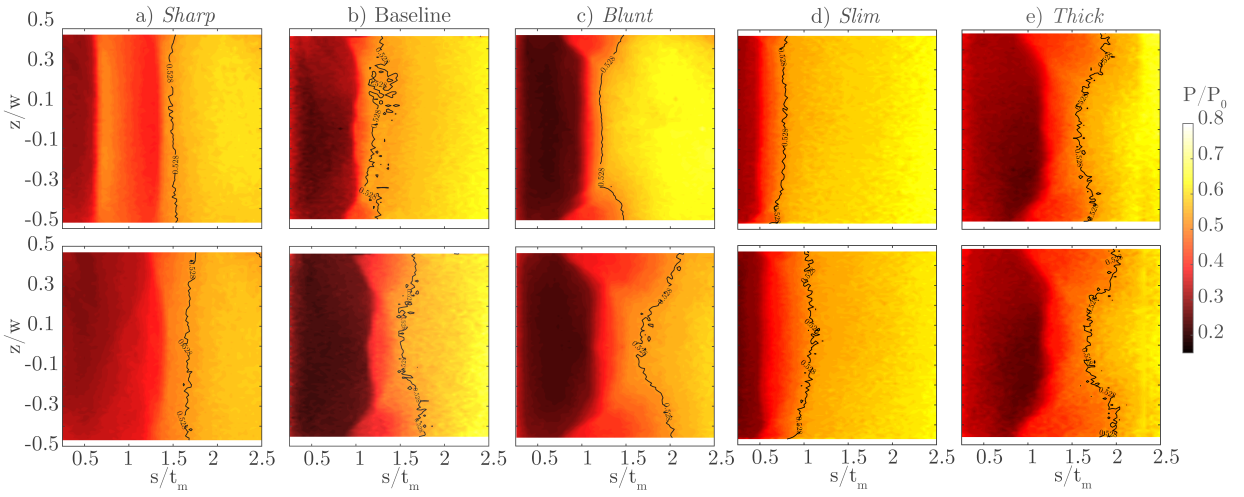


**Fig. 7 Wall pressure estimated using PSP for the five shapes considered at 23° for the reference $\dot{m}_u$ (top) and +15% increment (bottom). Black line is the sonic line.**

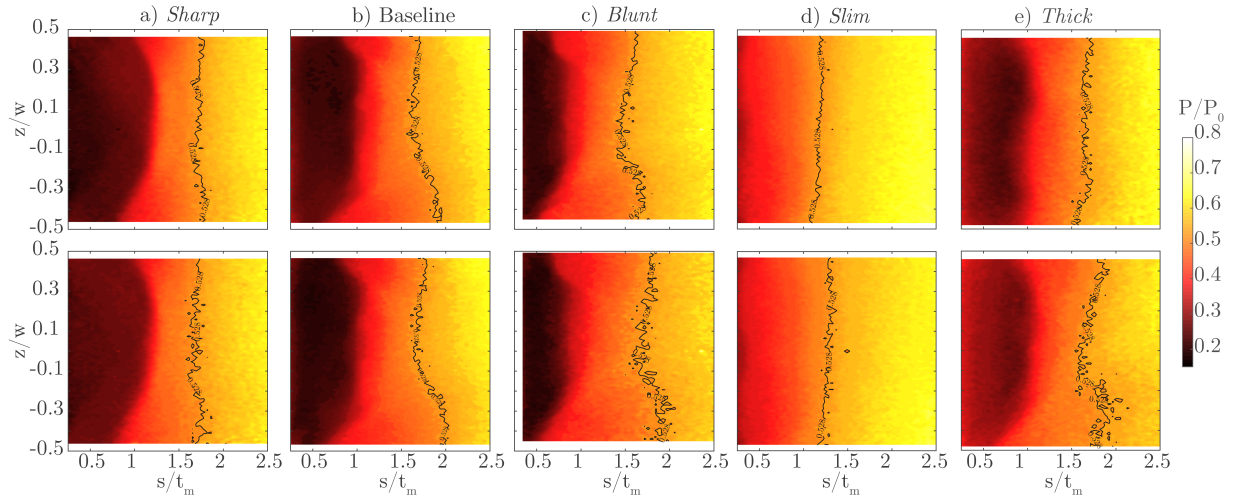


**Fig. 8 Wall pressure estimated using PSP for the five shapes considered at 25° for the reference $\dot{m}_u$ (top) and +15% increment (bottom). Black line is the sonic line.**

at 25°, reflect the largely separated flow near the highlight of the *slim* lip. For the *thick* lip, the onset of pressure rise is found marginally upstream compared to the reference incidence. The pressure smearing is comparable to the baseline.

From Figure 9, it appears that lip shape has a strong effect on both the peak isentropic Mach number (low pressure) and position of the shock wave. In order to assess the effect of the imposed pressure distribution on the boundary layer downstream of the interaction, velocity measurements are taken at the plane where an engine face would sit. This is slightly aft compared to the Aerodynamic Interface Plane, conventionally defined as slightly upstream of the fan plane. As shown in Figure 10, this location, referred to as the *Virtual Engine Plane* (*VEP*), is at x=2.4t$_m$. Measurements are shown for all shapes and incidences in Figure 10 normalised by their thickness $\delta$ and velocity at the boundary layer edge $U_e$. The boundary layer integral properties obtained from the data in Figure 10 are summarised in Table 4 and Table 5

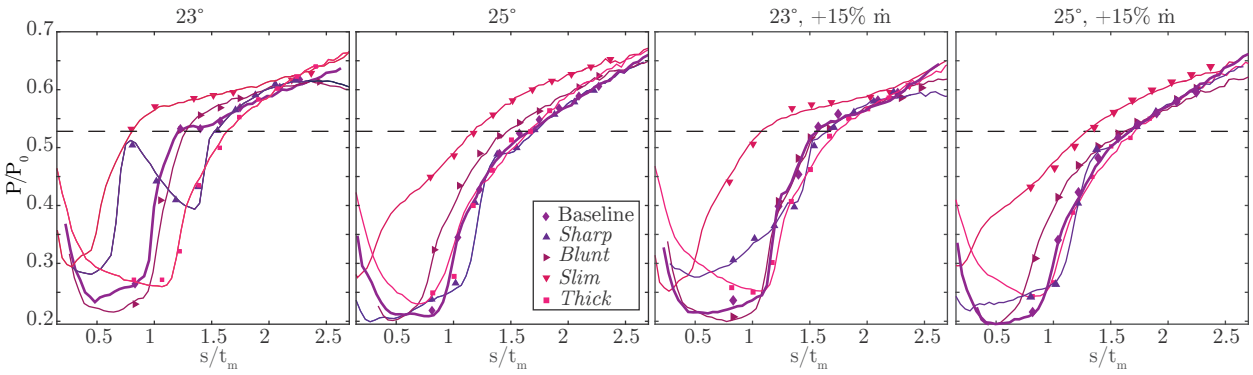


**Fig. 9 Centre-span pressure (solid line: PSP; symbols: transducer values) for each lip at two incidence levels and upper channel mass flow rate values.**

for the baseline and the four variations respectively.

Overall, at the reference mass flow rate and at an incidence of 23°, looking at the shape factor, all shapes display a relatively healthy turbulent boundary layer. However, a few differences are noted across the different lips. In particular, the boundary layer over the *blunt* lip is almost twice as thick as the baseline. Moreover, the values of momentum and displacement thicknesses are 60% larger. However, the *blunt* lip displays one of the fullest velocity profiles, as reported in Table 5.

On the other hand, the shape factor for the *sharp* lip is the highest measured at $H_i$=1.578, compared to a baseline value of $H_i$=1.365. Despite the relatively high measured shape factor, the *sharp* lip momentum thickness is approximately 10% greater than the baseline value and amongst the lowest measured value. This would suggest a reduced extent of momentum losses despite the very large shape factor. This counter-intuitive behaviour could be explained if the terminal interaction over the *sharp* lip is assumed to be attached. This hypothesis is supported by the weak suction peak observed for the terminal compression in pressure measurements in Figure 9 (and Appendix A). In literature, the recovery of the velocity profile downstream of an attached interaction is generally reported as a more gradual process than behind separated SBLIs [17] and, in adverse pressure gradients, recovery can be expected to be delayed even further.

The boundary layers for the two aspect ratio variations are of similar thickness at the *VEP* and almost twice that of the baseline case. The integral parameters for the *thick* lip, reported in Table 5d reveal the greatest displacement and momentum thicknesses. For the *slim* lip, despite the highest aspect ratio lip has the lowest measured shape factor of $H_i = 1.291$, the values for $\delta_i^*$ and $\theta_i$ are still larger than the corresponding baseline values.

As the mass flow rate is increased whilst maintaining the incidence of 23°, $\delta$, $\theta_i$ and $\delta_i^*$ grow slightly for every lip, with the exception of the peculiar *sharp* lip. The boundary layer shape factor, on the other hand, decreases for both the baseline and the *sharp* lip at 23° incidence as the mass flow rate is increased. For all other lip shapes, $H_i$ is seen to increase with mass flow rate. The changes in integral parameters are however small.

At higher incidence the differences in boundary layer properties at the *VEP* for the different shapes are more

pronounced. The peculiarity of the *sharp* lip is confirmed as incidence is increased, as it can inferred from Table 5a: while both other geometries display a considerable boundary layer thickening accompanied by a deterioration of all integral properties as the incidence increases, the increase in boundary layer thickness $\delta$ for the *sharp* lip is just in excess of 10%. Furthermore, for the reference mass flow rate both displacement and momentum thicknesses are seen to decrease at higher incidence. The measured shape factor at 25° is lower than at 23° and below any other geometry at 25°.

The *thick* lip at 25° shows an increase in integral properties approaching 100% compared to the reference incidence, in line with the increases experienced by baseline and the *blunt* lip counterparts. At 25°, the slimmer lip integral parameters reflect the consequences of the largely distorted flow field seen in Schlieren images (Fig. 6) and PSP (Fig. 8). The boundary layer is the thickest measured across any shape. Similarly, at 25°, for the reference mass flow rate all integral parameters are also the highest measured values with a shape factor of $H_i = 1.983$.

At higher incidence, boundary layer thickness and integral properties show a minor increase with $\dot{m}_u$ for the baseline, the *thick* and the *sharp* profiles, while they appear to remain unchanged or decrease slightly for the blunter and slimmer nose. However, these are changes deemed within experimental accuracy. With exception of the *sharp* lip, at 25° shape factor increases slightly with $\dot{m}_u$.

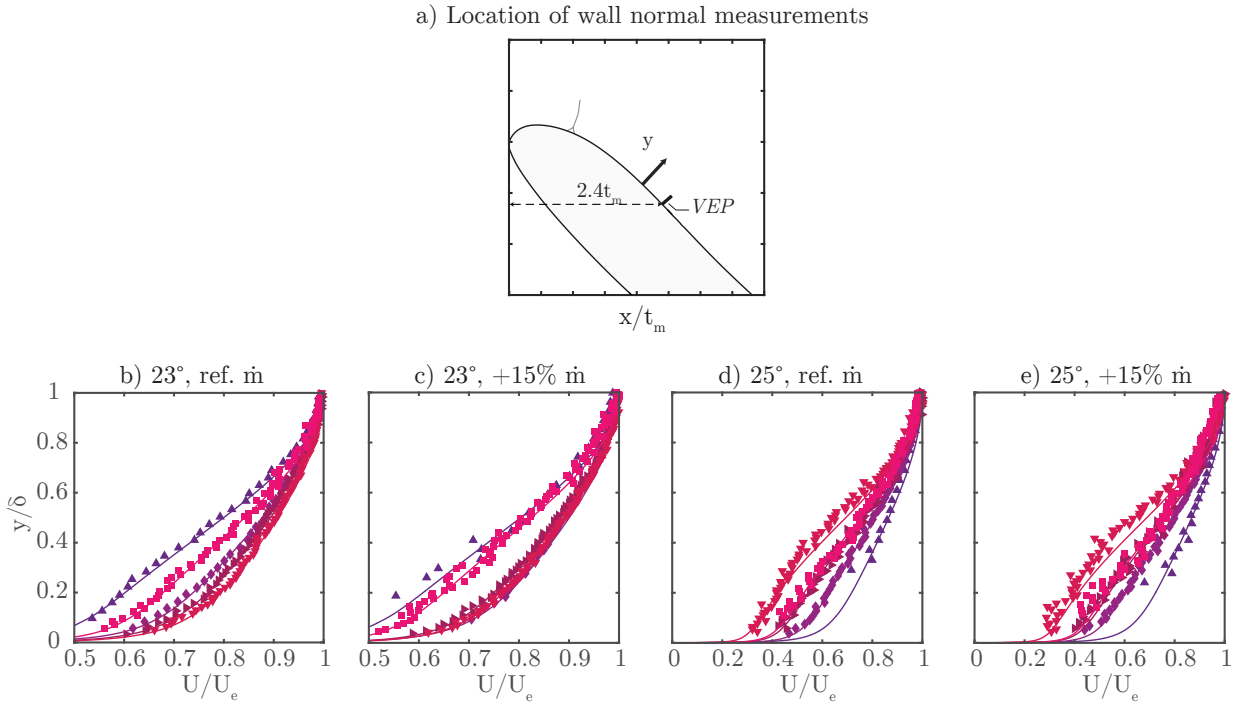


**Fig. 10 a) Location of the reference plane (*VEP*) corresponding to the nominal *engine* face. b-d) Normalised wall normal measurements at the reference plane for both incidence levels and mass flow rates. ▲ *Sharp*; ♦ Baseline; ► *Blunt*; ▼ *Slim*; ■ *Thick*.**

**Table 4 Incompressible boundary layer parameters for the baseline lip at the *VEP*.**

| $\alpha(^\circ)$ | $\dot{m}_u$ | $\delta/t_m$ | $\delta_i^*/t_m$ | $\theta_i/t_m$ | $H_i$ |
|---|---|---|---|---|---|
| 23 | Ref. | 0.0727 | 0.0109 | 0.0080 | 1.365 |
| | +15% | 0.0857 | 0.0109 | 0.0083 | 1.314 |
| 25 | Ref. | 0.162 | 0.0341 | 0.0224 | 1.521 |
| | +15% | 0.178 | 0.0399 | 0.0255 | 1.563 |

**Table 5 Incompressible boundary layer parameters for the four lip geometries considered at the *VEP*.**

**(a) *Sharp***

| $\alpha(^\circ)$ | $\dot{m}_u$ | $\delta/t_m$ | $\delta_i^*/t_m$ | $\theta_i/t_m$ | $H_i$ |
|---|---|---|---|---|---|
| 23 | Ref. | 0.063 | 0.0141 | 0.0089 | 1.578 |
| | +15% | 0.0533 | 0.0118 | 0.0075 | 1.569 |
| 25 | Ref. | 0.0706 | 0.0114 | 0.0082 | 1.393 |
| | +15% | 0.0844 | 0.0133 | 0.0097 | 1.382 |

**(b) *Blunt***

| $\alpha(^\circ)$ | $\dot{m}_u$ | $\delta/t_m$ | $\delta_i^*/t_m$ | $\theta_i/t_m$ | $H_i$ |
|---|---|---|---|---|---|
| 23 | Ref. | 0.126 | 0.0169 | 0.0128 | 1.320 |
| | +15% | 0.162 | 0.0233 | 0.0174 | 1.338 |
| 25 | Ref. | 0.257 | 0.0659 | 0.0393 | 1.677 |
| | +15% | 0.251 | 0.0646 | 0.0383 | 1.685 |

**(c) *Slim***

| $\alpha(^\circ)$ | $\dot{m}_u$ | $\delta/t_m$ | $\delta_i^*/t_m$ | $\theta_i/t_m$ | $H_i$ |
|---|---|---|---|---|---|
| 23 | Ref. | 0.135 | 0.0162 | 0.0125 | 1.291 |
| | +15% | 0.166 | 0.0221 | 0.0168 | 1.316 |
| 25 | Ref. | 0.297 | 0.0953 | 0.0481 | 1.983 |
| | +15% | 0.293 | 0.0954 | 0.0475 | 2.008 |

**(d) *Thick***

| $\alpha(^\circ)$ | $\dot{m}_u$ | $\delta/t_m$ | $\delta_i^*/t_m$ | $\theta_i/t_m$ | $H_i$ |
|---|---|---|---|---|---|
| 23 | Ref. | 0.1403 | 0.0255 | 0.0178 | 1.437 |
| | +15% | 0.173 | 0.0342 | 0.0231 | 1.480 |
| 25 | Ref. | 0.2036 | 0.0537 | 0.0314 | 1.713 |
| | +15% | 0.216 | 0.0572 | 0.0333 | 1.715 |

## IV. Factors influencing intake performance

The purpose of an intake is, by definition, to provide good quality flow at the engine face or, in other words, a thin and full boundary layer across the operating envelope. Ultimately, the boundary layer development depends primarily on the imposed pressure distribution. Along the lips investigated here, several regions of characteristic pressure gradients are identified: strongly favourable around the nose; a narrow re-compression region ahead of the shock; the shock pressure jump; the rise in pressure in the diffuser between the shock and the *VEP*. In order to determine whether one of these regions has a more dominant role, this section explores correlations between different parameters, concentrating on those deemed most likely to affect the boundary layer development: the strong adverse pressure gradient regions.

Figure 11a schematically depicts the main adverse pressure gradient regions and presents a typical centre-span pressure rise. The total pressure rise is the delta between the minimum pressure (peak isentropic Mach number) and the value at the *VEP*. The pressure rise across the normal shock, indicative of shock strength, cannot be determined exactly due to the smearing of the pressure rise in the wall region due to the interaction. Therefore, the shock $\Delta$P is approximated as the difference between the isentropic sonic line, where $P/P_0 = 0.528$, and the value at the pressure rise onset. The latter is taken at the point where the pressure gradients show an upward kink. The pressure rise in the

diffuser is the subsequent increase between the sonic value and the pressure measured at the *VEP*. The interaction length $L^*$ is taken as the stream-wise distance between the pressure rise onset and the isentropic sonic line. Both $\dot{m}_u$ values and incidence conditions are used for the correlations.

A special definition is required by the *sharp* lip at 23° incidence and reference $\dot{m}_u$. The pressure and pressure gradient distributions are shown in Figure 11b. In §III.A, this lip was found to result in a multiple shock system. The small shock in the immediate proximity of the highlight could not be resolved due to poor optical access and only the two downstream shocks are taken into account. As shown in Figure 11b, the interaction length here is taken as the sum of the two individual interaction lengths. However, since the pressure does not reach the sonic value, $L^*$ for the first shock has been defined as the distance between the pressure rise onset and the point of maximum pressure before the re-expansion. The shock pressure jump is also taken as the sum of the individual pressure rises across the two shocks. This relies on the hypotheses that the boundary layer does not have time to recover fully from the first shock wave before the second compression. Nonetheless, due to the different flow topology compared to the other lips, defined by multiple shock-boundary interactions, the results from the *sharp* lip ought to be treated with caution.

The main indicator of aerodynamic performance is chosen to be the momentum thickness $\theta_i$ at the *VEP*, being a measure of lost momentum. Shape factor $\mathrm{H}_i$ and boundary layer thickness $\delta$ are also considered.

Figure 12 shows the variation of $\delta, \theta_i$ and $\mathrm{H}_i$ with total pressure rise. Each shape is assigned a different symbol as indicated in the caption. Considerable scatter is present and no obvious trend is observed, suggesting no strong correlation.

The influence of $\Delta P_{shock}$ is presented in Figure 13. It can be seen how severely deteriorated boundary layer parameters are generally associated with a stronger shock wave. However a significant amount of scatter suggests no meaningful correlation with the shock strength, which is somewhat surprising. In particular, a number of shapes characterised by the same shock pressure jump have drastically different values for $\delta, \theta_i$ and $\mathrm{H}_i$ at the *VEP*.

Figure 14, on the other hand, shows the correlation between the boundary layer parameters and the pressure rise in the diffuser. Although it can be noted that higher values of $\theta_i$, $\delta$ and $\mathrm{H}_i$ are generally associated with a greater diffuser pressure rise, the scatter is significant and no strong correlation is observed.

Figure 15, on the other hand, shows the correlation between the boundary layer integral parameters and the interaction length $L^*$. A progressive deterioration of the integral parameters with a higher interaction length is seen. Recalling that a more smeared pressure rise (higher $L^*$) is generally a symptom of an increased separation, it appears logical that, as the size of separation increases, the downstream flow reflects increased losses. Normally, on a flat plate, shock strength and separation size could be expected to be linked. However, the scatter in Figure 16a, which shows little correlation between $L^*$ and $\Delta P_{shock}$, suggests this not to be the case. Thus, there seems to be some other factors affecting the separation size.

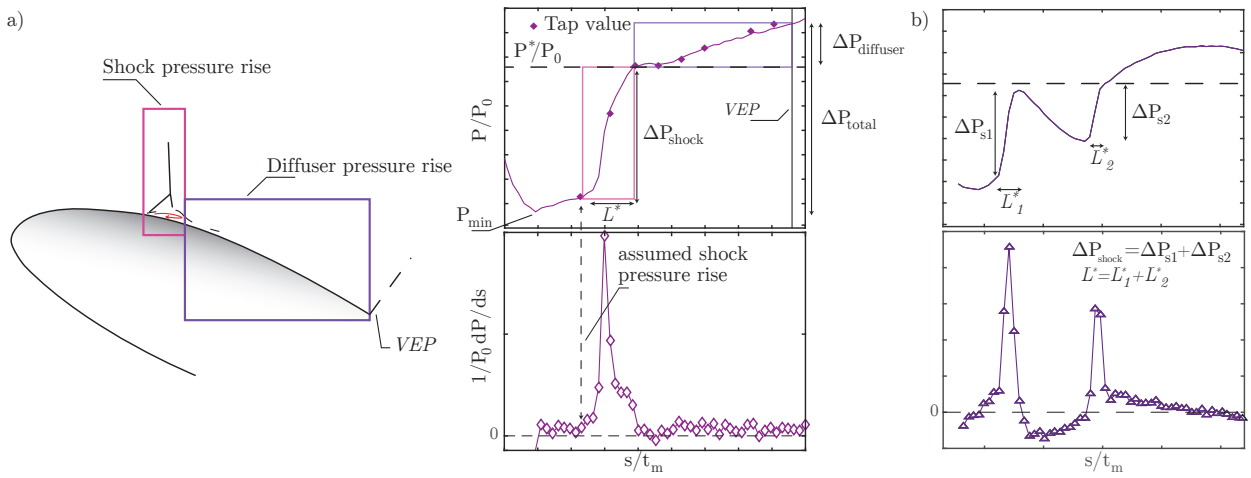


**Fig. 11 a) Definition of the pressure rise stages along the lower lip and of the interaction length $L^*$. b) Shock pressure rise and $L^*$ definitions for the peculiar sharp lip at 23°.**

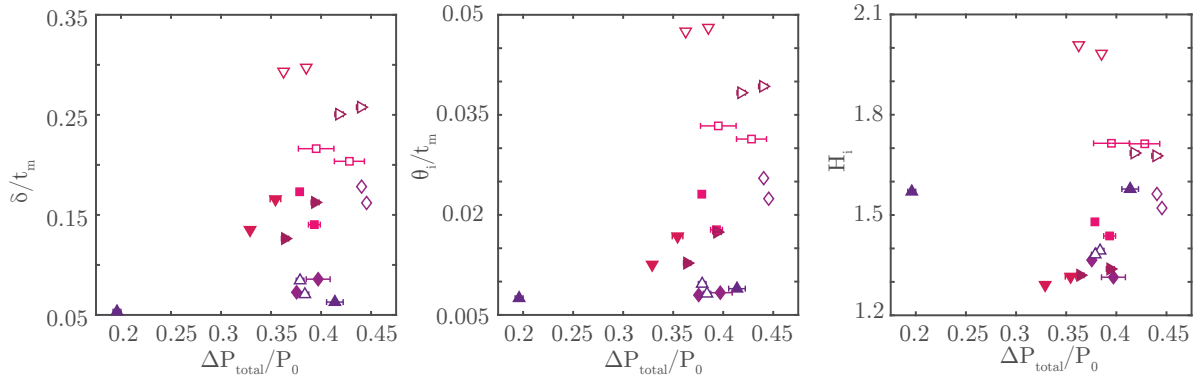


**Fig. 12 Variation of selected boundary layer properties at the *VEP* with total pressure jump. ▲ *Sharp*; ♦ Baseline; ▶ *Blunt*; ▼ *Slim*; ■ *Thick*. Open symbols: 25°.**

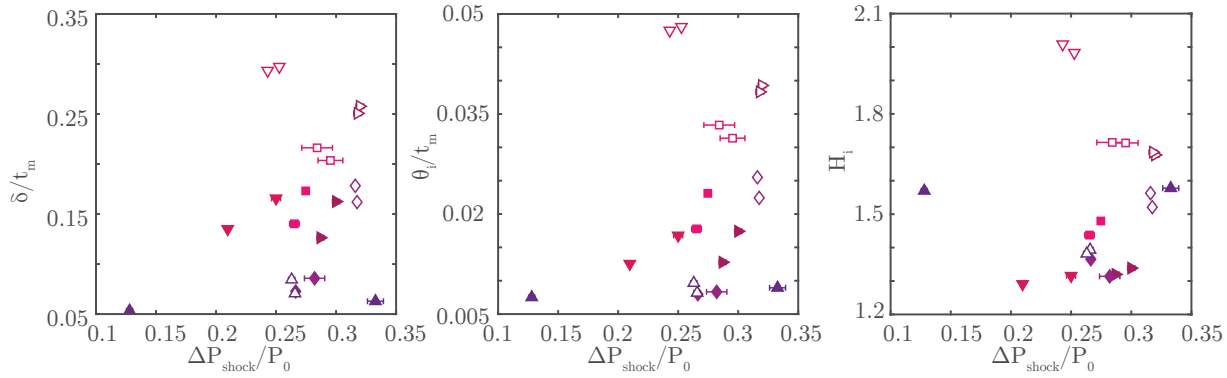


**Fig. 13 Variation of selected boundary layer properties at the *VEP* with shock pressure jump. ▲ *Sharp*; ♦ Baseline; ▶ *Blunt*; ▼ *Slim*; ■ *Thick*. Open symbols: 25°.**

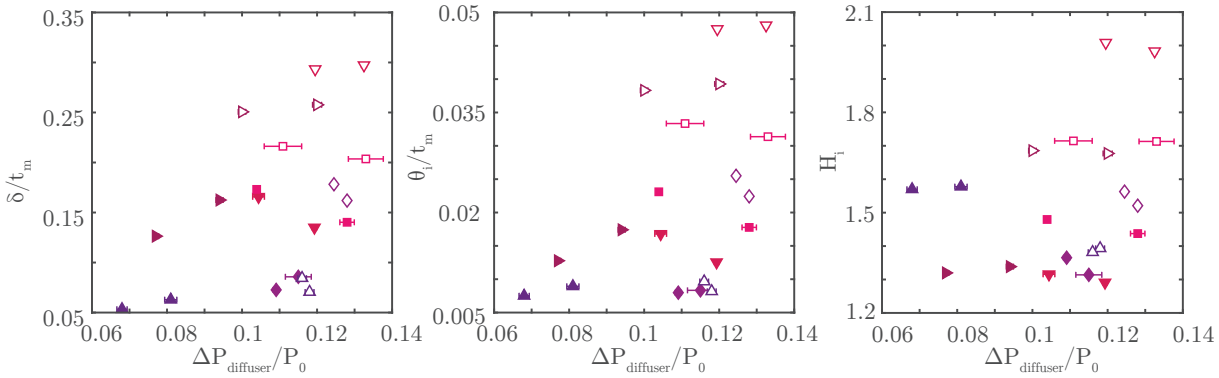


**Fig. 14 Variation of selected boundary layer properties at the *VEP* with diffuser pressure jump. ▲ *Sharp*; ♦ Baseline; ► *Blunt*; ▼ *Slim*; ■ *Thick*. Open symbols: 25°.**

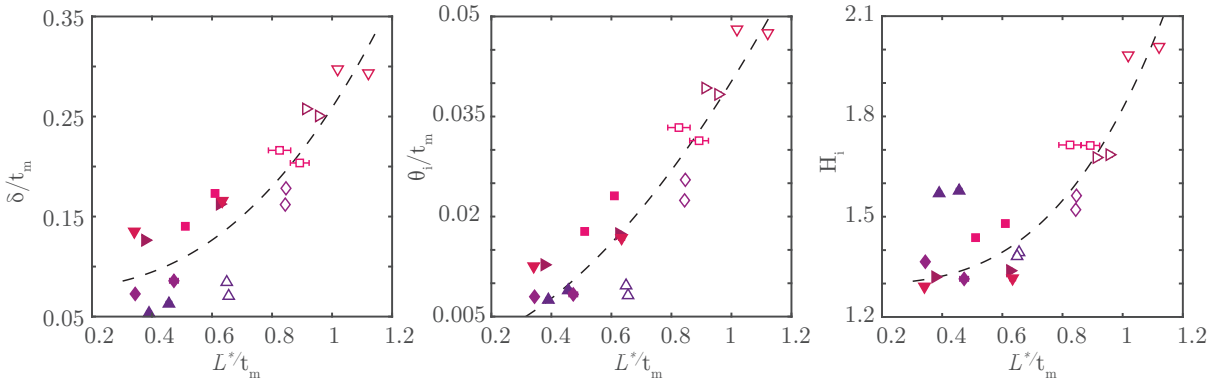


**Fig. 15 Variation of selected boundary layer properties at the *VEP* with interaction length $L^*$. ▲ *Sharp*; ♦ Baseline; ► *Blunt*; ▼ *Slim*; ■ *Thick*. Open symbols: 25°.**

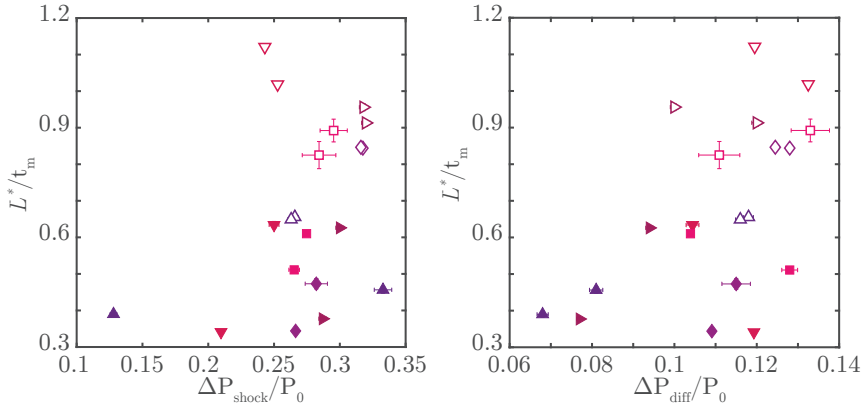


**Fig. 16 a) Variation of $L^*$ with shock pressure jump. b) Variation of $L^*$ with diffuser pressure rise. ▲ *Sharp*; ♦ Baseline; ▲ *Sharp*; ♦ Baseline; ► *Blunt*; ▼ *Slim*; ■ *Thick*. Open symbols: 25°.**

Similarly, Figure 16b, which depicts the relationship between diffuser pressure rise and interaction length, shows no significant correlation between the two. However, despite the large scatter, large values of $L^*$ are generally associated with a large diffuser pressure rise.

Based on this evidence, it can be cautiously concluded that the downstream boundary layer development is mostly affected by the shock-induced separation. Interestingly, the separation length appears to be nearly independent of shock strength. The correlation shows substantial scatter, however, the subsequent pressure rise in the diffuser is expected to further delay flow reattachment after the shock. Furthermore, the diffuser pressure rise is also likely to have a direct effect on the boundary layer development.

An important consequence of a less full velocity profile is an increase in core flow deflection. This results in a *de-cambering* of the inlet lip, which in turns may affect the shock position. Observing the values of displacement thickness in Table 5, it is noted that those lip characterised by a large value of $\delta_i^*$ at higher incidence, such as the *slim*, *thick*, and *blunt* lips, are also those that display a pronounced upstream motion of the shock compared to the reference incidence. Ultimately, this upstream motion of the shock might signify the inlet is approaching highlight separation.

Although a shock located more upstream is likely to be weaker, shock strength has not been found to have a significant impact on the boundary layer at the *VEP* in the presence of severe diffusion downstream of the shock. As a result, extra care is necessary when designing slimmer lips, which favour a terminal shock to be located very close to the highlight, leading to a greater portion of the pressure rise to occur in the diffuser.

## V. Conclusion

A novel rig has been used to investigate the shock-wave boundary layer interaction occurring over the lower lip of transonic engine intakes at incidence. Alongside a baseline inlet shape, four more profiles have been investigated.

For the reference intake shape, the flow field around the lower lip during on-design take-off conditions was found to be relatively benign, with minimal shock-induced separation. As incidence is increased by 2°, from the reference value of 23°, this separation gets noticeably larger, unsteadiness develops and the downstream boundary layer velocity profile is more distorted.

The parametric investigation revealed a significant effect of lip shape on the SBLI.

The relationship between the boundary layer state at the *VEP* and a number of parameters, such as shock strength, diffuser pressure rise and interaction length $L^*$ (indicative of the size of shock-induced separation) was explored. This was aimed at determining the main contributor to aerodynamic performance.

The most interesting correlation is found between a greater interaction length and larger momentum deficit downstream of the shock. Interestingly, this length is found to be nearly independent of shock strength. Correlation with the pressure rise in the diffuser downstream of the shock was also affected by large scatter. However, it is likely that a more severe diffusion immediately downstream a strong shock wave could delay re-attachment resulting in a greater separation length (thus causing high $L^*$ values), which is ultimately reflected in a greater momentum deficit $\theta_i$. No strong correlation between the boundary layer parameters downstream and the shock pressure jump is seen.

As intakes get larger, to allow for both ground clearance and a reduced parasitic drag during cruise, a thinner intake

is preferable. However, the findings of this research suggest that the consequences of this design choice might have negative repercussion on performance outside cruise, that is during climb or high thrust operations. In particular, a slimmer lip is found to potentially promote early onset of highlight separation as incidence increases. Although the shock Mach number observed for this shape is amongst the lowest recorded, the separation is the largest. This could be a result of the prolonged adverse effects of the downstream diffusion preventing flow reattachment and resulting in large momentum deficit and streamline deflection that might ultimately favour highlight stall. Thus, nacelle lower lip design should be aimed at controlling the shock position, avoiding a separated SBLI in regions dominated by strong diffusion. If a strong diffuser is necessary to more drastically reduce the flow speed ahead of the fan, then this should be kept away from the SBLI in order to avoid delaying the boundary layer reattachment. Naturally, these findings ought to be weighted along beneficial effects of such profiles during cruise, of which assessment was far from the scope of this investigation.

# Appendix

### A. *Sharp* lip oil flow visualisation

Figure 17 shows oil flow visualisation over the sharp lip. A first separation line is seen near the highlight. This corresponds to the first interaction observed in the Schlieren. A small oil accumulation, indicating incipient separation, is seen in correspondence to the second SBLI. The final compression, occurring via the third and last shock-wave, is barely visible, implying that this last interaction might be attached.

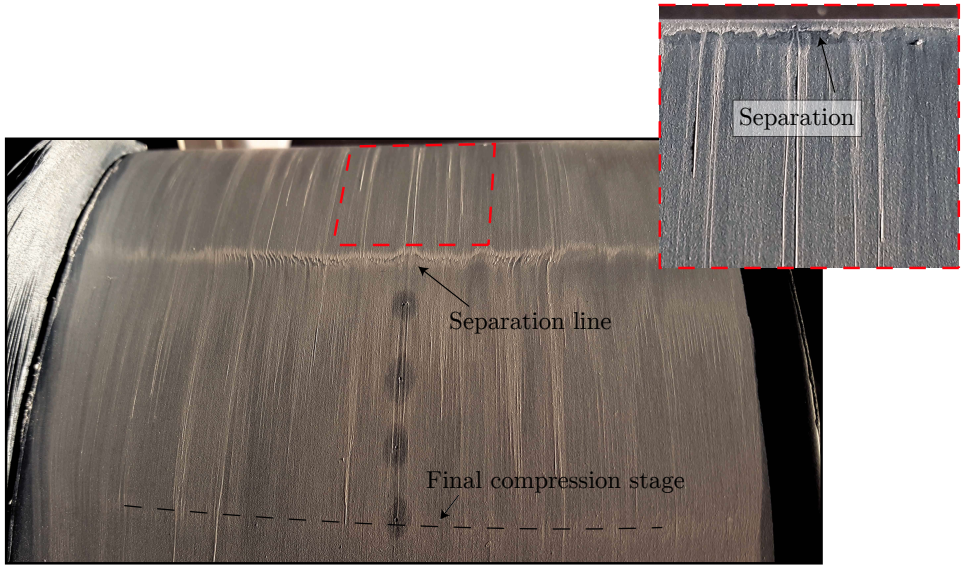


**Fig. 17 Oil flow visualisation over the *Sharp* lip at 23° and reference $\dot{m}_u$. Detail of the first interaction is shown in the top right corner.**

## Acknowledgements

The authors wish to acknowledge Dave Martin, Sam Flint, Anthony Luckett and John Hazlewood for operating the CUED blow-down wind tunnel. Moreover, they would like to thank Rolls Royce Plc, the Engineering and Physical Sciences Research Council (EPSRC) and the National Wind Tunnel Facility for invaluable (NWTF) contribution towards this research.

## References

[1] MILLER, B. A., and DASTOLI, B. J., "Effect of entry lip design on aerodynamics and acoustics of high-throat- Mach-number inlets for the quiet, clean, short-haul experimental engine." *NASA Technical Paper 3222*, 1975.

[2] JAKUBOWSKI, A. K., and LUIDENS, R., "Internal cowl-separation at high incidence angles," *13th Aerospace Sciences Meeting. Pasadena,CA,USA.*, 1975. doi:10.2514/6.1975-64.

[3] ALBERS, J. A., and STOCKMAN, N. O., "Calculation Procedures for Potential and Viscous Flow Solution for Engine Inlets," *NASA Technical Memorandum 71457*, 1974.

[4] LUIDENS, R. W., and ABBOTT, J. M., "Incidence angle bounds for lip flow separation of three 13.97-centimetre-diameter inlets," Tech. rep., NASA TM X-3551, 1976.

[5] COSCHIGNANO, A., BABINSKY, H., SHEAF, C., and ZAMBONI, G., "Normal Shock-Boundary Layer Interactions in Transonic Intakes at High Incidence," *AIAA Journal (Articles in Advance)*, Vol. 0, No. 0, 2019. doi:10.2514/1.J058054.

[6] MAKUNI, T. E., BABINSKY, H., SLABY, M., and SHEAF, C. T., "Shock Wave-Boundary-Layer Interactions in Subsonic Intakes at High Incidence," *53rd AIAA Aerospace Sciences Meeting. January*, 2015. doi:10.2514/6.2015-0067.

[7] MEIER, H., "Measuring techniques for compressible turbulent boundary layers," *NASA STI/Recon Technical Report N. 79*, 1977.

[8] GREGORY, J. W., ASAI, K., KAMEDA, M., LIU, T., and SULLIVAN, J. P., "A review of pressure-sensitive paint for high-speed and unsteady aerodynamics," *Proc. IMechE Vol. 222 Part G: J. Aerospace Engineering*, 2007. doi:10.1243/09544100JAERO243.

[9] COLLISS, S. P., *Vortical structures on three-dimensional shock control bumps*, PhD Thesis, University of Cambridge, 2014.

[10] SHAKAL, J., and TROOLIN, D., "Accuracy, Resolution, and Repeatability of Powersight PDPA and LDV Systems," *TSI Technical Note P/N 5001519*, 2013.

[11] MCLAUGHLIN, D. K., and TIEDERMAN, W. G., "Biasing correction for individual realization of laser anemometer measurements in turbulent flows," *Physics of Fluids*, Vol. 16, No. 1973, 1973, pp. 2082–2088. doi:10.1063/1.1694269.

[12] BUCHHAVE, P., and GEORGE, W. J., "Bias corrections in turbulence measurements by the laser Doppler anemometer," Tech. rep., Turbulence Research Laboratory, State University of New York at Buffalo, 1978.

[13] SUN, C., and CHILDS, M. E., "A modified wall wake velocity profile for turbulent compressible boundary layers." *Journal of Aircraft*, Vol. 10, No. 6, 1973, pp. 381–383. doi:10.2514/3.44376.

[14] COLES, D., "The law of the wake in the turbulent boundary layer," *Journal of Fluid Mechanics*, Vol. 1, No. 02, 1956, p. 191. doi:10.1017/S0022112056000135.

[15] MUSKER, A. J., "Explicit Expression for the Smooth Wall Velocity Distribution in a Turbulent Boundary Layer," *AIAA Journal*, Vol. 17, No. 6, 1979, pp. 655–657. doi:10.2514/3.61193.

[16] TITCHENER, N., COLLISS, S., and BABINSKY, H., "On the calculation of boundary-layer parameters from discrete data," *Experiments in Fluids*, Vol. 56, No. 8, 2015, pp. 1–18. doi:10.1007/s00348-015-2024-5.

[17] BABINSKY, H., and HARVEY, J. K., *Shock-wave-Boundary layer Interactions*, Cambridge University Press, 2011. doi: 10.1017/CBO9780511842757.